ELSEVIER

Chemical Geology 205 (2004) 17–36

CHEMICAL GEOLOGY
INCLUDING
ISOTOPE GEOSCIENCE

www.elsevier.com/locate/chemgeo

Cyclic fluid infiltration in structurally controlled Ag–Pb–Cu occurrences (Schladming, Eastern Alps)

Jörg Robl*, Harald Fritz, Kurt Stüwe, Franz Bernhard

Institut für Geologie und Paläontologie, Universität Graz, Heinrichstr, 26 A-8010 Graz, Austria

Received 19 September 2002; accepted 28 November 2003

Abstract

Polysulphide occurrences in the Schladming Crystalline Complex, Eastern Alps, are associated with the intersection of moderately N-dipping shear zones (Type-I structures) and NW–SE and NE–SW trending steep faults (Type-II structures). Geochemical and mineralogical profiling across the Type-I structures shows progressive mineral alteration (feldspar breakdown, silicification, sericitisation) from the margin to the center. These observations are best interpreted by an external acidic fluid infiltrating these structures. Such alteration halos in deep-seated structures are excellent leaching sites and transport channels for available metals. However, precipitation of ore took place at the contact with carbonates where metal-bearing complexes became unstable as a result of fluid neutralisation. The origin of this carbonate is linked with Type-II structures showing distinct carbonatisation but no wall rock alteration. It is therefore suggested that the ore occurrences in Type-I and Type-II structures were formed during the cyclic infiltration of an acidic and a CO_2-bearing fluid. Fluid inclusions from quartz–carbonate–ore veins are consistent with this interpretation. *PT* estimates and the orientation of shear zones and faults are consistent with the geodynamic setting of Cretaceous cooling and exhumation of the Austroalpine realm east of the Tauern window. The exhumation of the Schladming Crystalline Complex is therefore interpreted as the setting for a cyclic process of increased fluid pressure, vein opening, fluid infiltration, ore precipitation and vein closure.

Keywords: Ore deposits; Cyclic fluid infiltration; Cretaceous tectonics; Schladming Crystalline Complex

1. Introduction

Shear zone hosted gold, base metal and polysulphide deposits are often hosted by rocks of greenschist metamorphic grade (Goldfarb et al., 1986; Stüwe, 1998; Craw et al., 1999). For many of these deposits, it is well established that acidic fluids acted as transport agents for the metal-bearing fluids (see summary by Seward and Barnes, 1997). However, there has been some discussions on the origin of ore-forming metals and fluids in these deposits. Some authors have argued that extremely low concentrations of metals in crustal rocks imply that the ore-bearing fluids must have been derived from an external source rock (Glasson and Keays, 1978). In support of this argument, it has been observed that many deposits formed after the greenschist metamorphic peak of their host rocks, so that it is difficult to invoke prograde dewatering as a source for local metamorphic fluids. Instead, it has been suggested that the ore-

* Corresponding author.
E-mail address: joerg.robl@uni-graz.at (J. Robl).

0009-2541/$ - see front matter © 2004 Elsevier B.V. All rights reserved.
doi:10.1016/j.chemgeo.2003.11.018

bearing fluids must be derived from a magmatic source at depth (Groves, 1993). Others have argued that the post-metamorphic peak formation of these deposits can be explained by the asynchronous nature of metamorphism at different depths (Stüwe, 1998; Pettke et al., 2000). High fluid–rock ratios can be explained with cyclic processes and focusing of metamorphic fluids over large length scales (Peacock, 1989). Cyclic pumping processes by fault valve action have been suggested by Sibson et al. (1988) and Nguyen et al. (1998).

Despite many similarities of these deposits, the precipitation mechanisms of ore appear to be highly variable. They include fluid reduction during fluid–rock interaction (Mikucki, 1998), fluid neutralisation (Reed, 1997; McCuaig and Kerrich, 1998) and even bacterial sulphide reduction (Bechtel et al., 2002).

In this paper we present an example of a shear zone hosted polysulphide mineralisations in the Schladming Crystalline in the Eastern Alps, where it can be shown that the ore precipitates at the contact with carbonates that were precipitated roughly simultaneously by an independent fluid. It is also shown that the leaching and precipitation mechanism is likely to have occurred cyclically, so that our study provides an illustration of successive ore enrichment processes in a well-constrained geological setting. The Schladming area is a historical mining district within the Austroalpine nappe complex where mining activities go back to the Middle Ages (Weiss, 1987). Based on a systematic study of tectonic structures, geochemistry and fluid inclusions in several old mines, a model for transport and precipitation of metals within shear zones and faults is presented. The proposed scenario of cyclic fluid infiltration is discussed in the frame of Upper Cretaceous extension and exhumation of the region.

2. Geological setting

The Schladming Crystalline Complex is part of the Middle Austroalpine nappe complex in the Eastern Alps (Neubauer and Frisch, 1993) (Fig. 1). Immediately north of the study area, a major Miocene fault system (SEMP, Fig. 1, inset) separates the Middle Austroalpine from the Upper Austroalpine tectonic units (Wang and Neubauer, 1997; Frisch et al., 1998). In the western part of the investigated area, Lower Austroalpine basement units and Permo-Mesozoic cover sediments are tectonically imbricated and folded together with the Schladming Crystalline (Formanek, 1963; Matura, 1987). The crystalline basement itself is composed of polymetamorphosed micaschists and gneisses that suffered Variscan amphibolite grade metamorphism (Slapansky and Frank, 1987; Neubauer and Frisch, 1993). This rock suite was intruded by late to post-Variscan (Schermaier et al., 1997) granites, granodiorites, diorites and gabbros. Phyllite—interpreted as Permo-Mesozoic cover sediments (Matura, 1987)—occurs as slices within and as a distinct unit underlying the Schladming Crystalline (Fig. 1b and c). Because of the structural position of these inferred Permo-Mesozoic quartz phyllites in the Variscan basement rocks, fold and thrust tectonics during Alpine times have been suggested for the region (Slapansky and Frank, 1987), but it will be shown later that at least some of these zones represent high-deformation zones within the crystalline basement rather than distinct Permo-Triassic units. During the Alpine metamorphic cycle, the region suffered strong metamorphic overprint at upper greenschist facies metamorphic grade. Continuous cooling of the Schladming Crystalline Complex from above ca. 350 °C started in the Cretaceous (Hejl, 1997; Thöni, 1999) and is related to late Cretaceous extension, well-described from comparable Middle Austroalpine units elsewhere in the Eastern Alps (Neubauer et al., 1995).

Throughout the Schladming Crystalline, mineralisations of Ag, Cu and Pb sulphides are found in quartz–carbonate veins in association with the quartz phyllites. These quartz veins are typically 10–30 cm wide but may be highly deformed so that they form sets of millimeter-wide stringers aligned in the sheared fabric. These veins are highly mineralized and form concentrated zones up to several hundreds of meters in length and we refer to them here as "ore bodies". They were mined for their base metals until early last century. The quartz veins occur in different stages of deformation indicting that they formed over a prolonged period of shear zone activity. In this study three mineralisations were investigated. These are here referred to as the Crombach, Bromries and Rossblei mineralisations (Fig. 1). For detailed description on former mining locations and ore phases, see

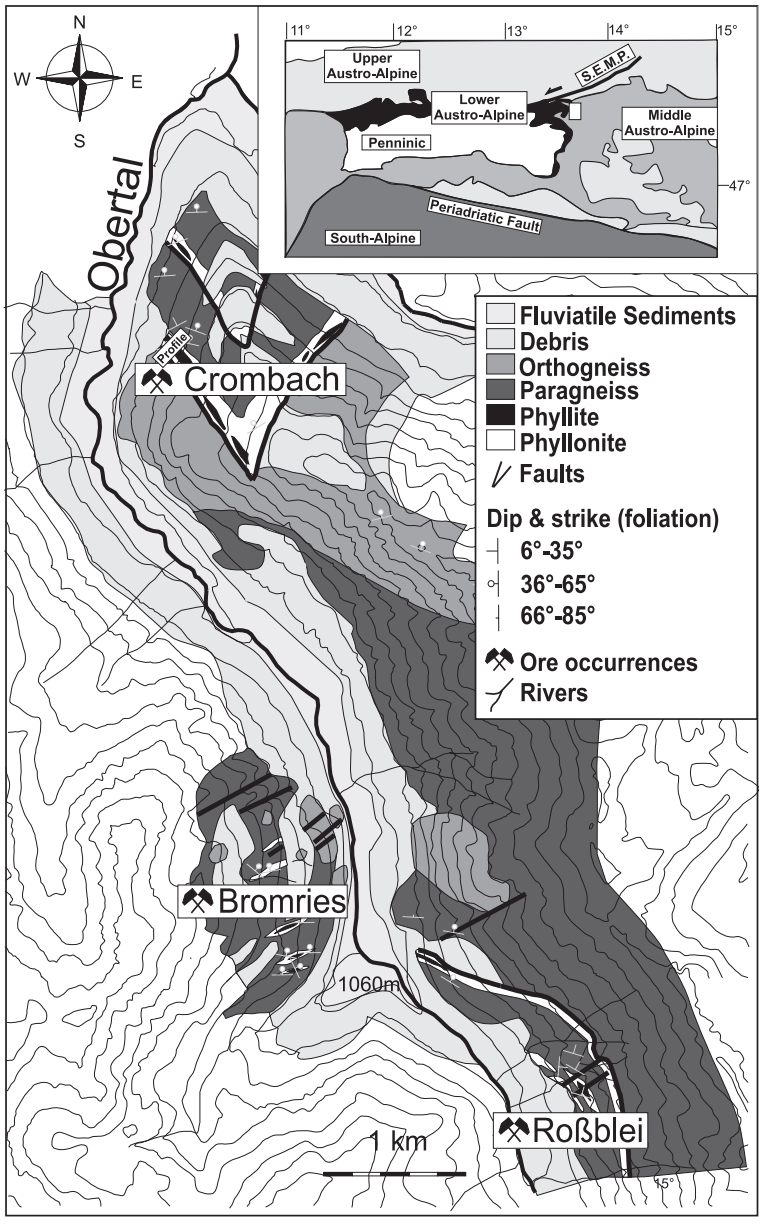

Fig. 1. Regional setting and location map of the investigated area the white box in the inset shows the position of the investigated area.; SEMP = Salzachtal–Ennstal–Mariazell–Puchberg Fault.

compilations by Friedrich (1975). The mineralisations belong to two different structural types. The Crombach occurrence is located in a west–east trending, gently north dipping shear zone (mapped as quartz phyllite zone by Mandl and Matura, 1995). In contrast, the ore occurrences of Rossblei and Bromries are located within steep bundles of northwest–southeast and northeast–southwest trending faults (Fig. 2). Both the Crombach and the Rossblei/Bromries type structures are common in the investigated area, but ore mineralisation is only found next the intersection of both structural elements. All ore bodies are close to or

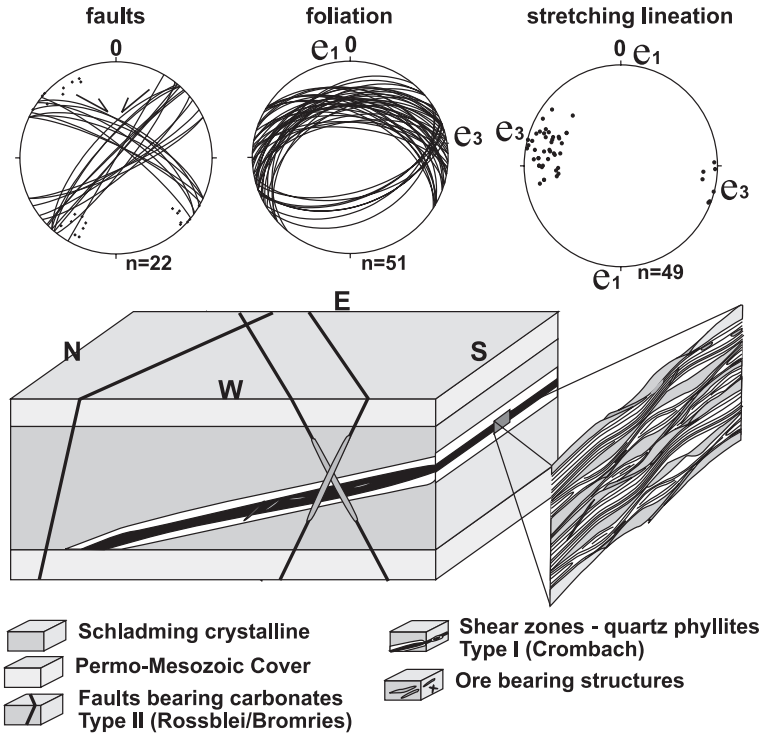

Fig. 2. Structural setting of the ore occurrences. The schematic block diagram shows the position of Eoalpine brittle and brittle–ductile structures. Faults, foliation and stretching lineation are shown as stereographic plots. e_1 and e_3 are the principle elongation directions, n is the number of measured data.

within quartz phyllite. Köppel et al. (1993) performed a Pb-isotope study of the mineralisations and suggested the metallogeny as a product of late Neoproterozoic to Mid-Ordovician active continental margin development. However, Pohl and Belocky (1999) argued for an origin during the Cretaceous metamorphic cycle. Certainly the orientation of the structures is consistent with the regional stress regime inferred for the Cretaceous.

3. Description of the ore-hosting structures

Both structures that play apparently an important role for the mineralisations were investigated for this study. Firstly, the structural characteristics of the west–east trending shear zones (Type-I structures) are discussed. These structures are well-exposed at Crombach and are characterized by a complicated succession of subzones. Their discussion forms the principal part of this paper. Then, the steep discrete conjugate fault zones (Type-II structures) are discussed. These structures are often filled by carbonate and are best exposed at Bromries and Rossblei.

3.1. Structural and mineralogical changes in Type-I structures

At Crombach, the quartz phyllite hosting the ore bodies displays all features of a typical mylonite zone within a granodiorite. This undeformed protolith consists of quartz, plagioclase and K-feldspar with minor muscovite, biotite and amphibole as well as accessory sphene and zircon. Some of the K-feldspars show minor sericitisation. The granodiorite exhibits magmatic textures including growth zoning, magmatic twinning of feldspar and interstitial quartz. The shear zone margins are not well-defined but a gradual mineralogical and structural transition from the undeformed granodiorite to the highly strained center of

the shear zone can be observed over a distance of several tens of meters. Ore bodies are hosted by quartz–carbonate veins in the shear zone. Vein density increases from the margins to the highly strained center of the shear zone. Veins that formed during late deformation increments occupy high angles to the foliation and contain stretched fibrous minerals, grown perpendicular to north–south trending vein margins. Earlier formed veins have rotated towards the direction of stretch and are boudinaged (Fig. 3). Textures and fabrics are compatible with deformation at greenschist facies metamorphic conditions.

Based on macroscopic features, three subzones are distinguished (Fig. 4). Subzone-A represents the ca. 50 m wide shear zone margin, subzone-B (ca. 30 m wide) is characterized by increasing strain and mineral alteration towards the shear zone center and subzone-C is the highly strained shear zone center itself (Fig. 4). Subzone-A and subzone-B are symmetrically arranged around subzone-C roughly 30 and 50 m wide, respectively. All subzones show evidence for different intensities of deformation in a shear zone. A mylonitic foliation is defined by S-C pattern and extensional crenulation cleavage fabrics, both coated

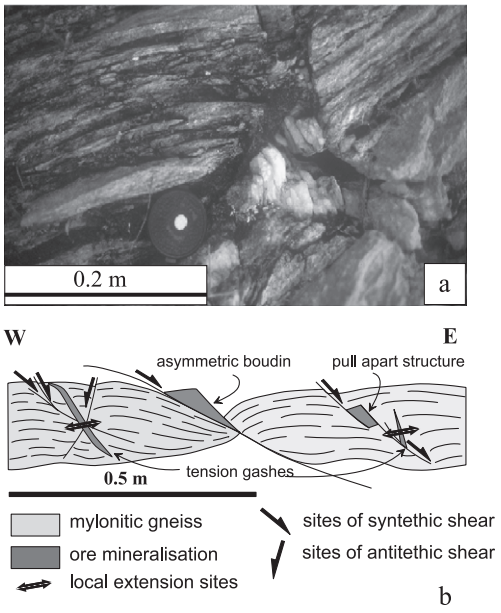

Fig. 3. (a) Mineralized boudin neck (subzone-C). (b) Tectonically controlled ore precipitation in the shear zone (subzone-C) during west–east stretch.

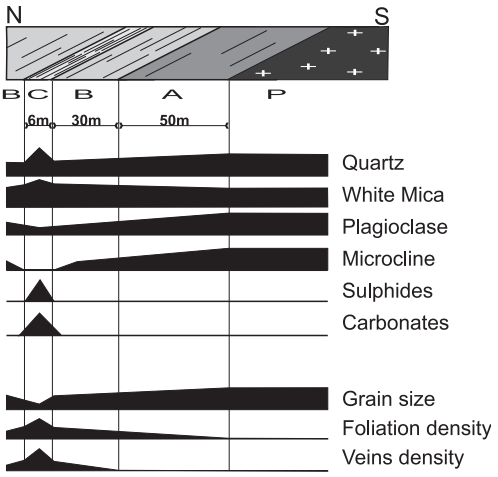

Fig. 4. Principle mineralogical and structural changes across the Crombach shear zone. A, B and C refer to the different subzones discussed in the text. P is the protolith. Note that subzone-A and subzone-B also occur on the north side of subzone-C (although this part is not shown here).

with newly grown mica. A pronounced, horizontal east–west oriented stretching lineation (Fig. 2) is defined by rods of quartz, mineral stretching and a shape preferred orientation of both feldspar and mica. Foliation boudinage and quartz-filled boudin necks formed during west–east stretching in the central, high strain domains of the shear zone (Fig. 3a). Heterogeneous strain distribution across the shear zone is evident from progressive grain size reduction and the increase of the density of newly formed foliation planes from marginal to the central shear zone. Typical mineral textures include plastic deformation of quartz and brittle behavior of feldspar. However, all ductile fabrics are also overprinted by brittle structures. These include sets of variably deformed and mineralized veins that display several stages of progressive deformation.

Subzone-A represents the margins of the shear zone. The subzone looks largely like the protolith (Fig. 5a) but shows some evidence for weak solid state flow. This includes undulatory extinction and deformation lamellae within quartz. K-feldspar and plagioclase show microfractures with sericite and epidote growth inside cracks. Stress-induced perthites and myrmekites are observed at the boundaries and within some grains. Some initial shear bands occur.

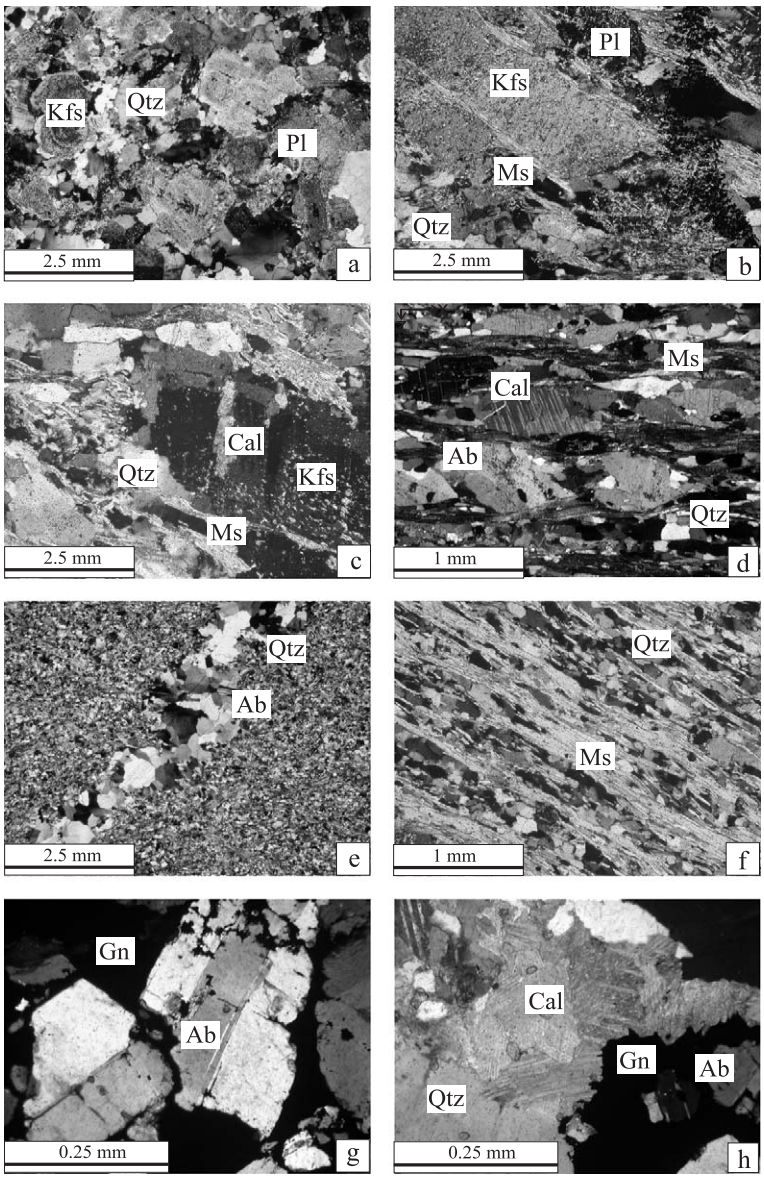

Fig. 5. (a) Subzone-A is characterized by weak deformation and initial break down of feldspar. (b) Subzone-B shows initial shear bands coated by mica. Quartz is recrystallised. (c) In the transition between subzone-B and subzone-C first appearance of carbonate in veins is observed. Subzone-C shows mylonitic fabrics with stretched carbonate and albite (d), veins with quartz and albite growths (e), and mylonites entirely composed of quartz and mica (f). (g) Newly grown fractured albite crystal in a ductile matrix of galena (Rossblei). (h) Calcite solution, fluid neutralisation and ore precipitation is indicated by the reaction front between galena and calcite (Rossblei). Mineral abbreviations after Kretz (1983).

Subzone-B is defined as the up to 30 m wide transition zone between subzone-A and the highly deformed central part of the shear zone. A penetrative foliation and pronounced stretching lineation are developed. Quartz grains show pronounced lattice and shape preferred orientation subparallel to the macroscopically observed stretching lineation. Relics of highly strained quartz grains are still preserved but

increasingly replaced by dynamically recrystallised subgrains (core mantle textures). Grain-boundary-migration crystallization and subgrain rotation features suggest dislocation glide and dislocation climb deformation mechanisms. Shear and extension veins within feldspar are common (Fig. 5b and c). Significant grain size reduction and the break down of feldspars produce a ductile appearance of the fabric. Across subzone-B an increase of sericite growth at the expense of feldspars is observed (Fig. 5b). K-feldspar disappears completely towards the center of the shear zone (subzone-C). Albite is formed at the expense of both plagioclase and K-feldspar and perthitisation along grain boundaries of K-feldspar may be observed. The occurrence of this perthitisation, mainly at the contact between rigid grains, indicates that this may be stress-induced. In contrast to subzone-A there is no epidote.

Subzone-C represents the ca. 6 m wide and highly strained center of the shear zone (Fig. 5d–f). The increase of sericite and quartz is significant in this zone so that almost the entire shear zone is composed of these two minerals (Fig. 5f). The only feldspar is albite which is progressively replaced by sericite, but feldspar is generally rare. However, some newly grown albite grows inside veins (Fig. 5e). An important mineralogical feature is the first appearance of carbonates and sulphides precipitated within veins. Deformation is penetrative down to grain scale (Fig. 4). Deformation induced layering, subparallel to the shear zone margins, can be led back to the alternation of discrete sericite bands with ribbon quartz. Quartz grains exhibit pronounced lattice preferred orientation but minor shape preferred orientation. An equi-granular pattern of dynamically recrystallised quartz with pinned boundaries next to mica layers developed by grain-boundary-migration crystallization. Numerous microboudinage structures (Fig. 5d), shear and extension veins suggest that strain was not entirely accommodated by ductile flow. Veins include newly grown fibrous quartz and albite.

3.2. Type-II structures

Type-II structures best exposed at the Rossblei and Bromries mineralisations and show completely different features (Friedrich, 1975). Although mylonitic fabrics similar to the Type-I structures occur within paragneisses in the vicinity of the ore bodies, the ore mineralisations occur in discrete steep fault zones and shear extension gashes with northwest–southeast orientation. Also, the ore bodies contain only little quartz, but massive carbonate. The large amount of carbonate that precipitated within the faults is important, since there are no carbonate-bearing rocks exposed elsewhere in the Schladming Crystalline. Sets of steeply dipping faults trend southwest–northeast and northwest–southeast (Fig. 2). The deformation is dominated by cataclastic flow within silicate minerals, including fracturing down to grain size scale. Calcite, which is sensitive to ductile flow at low temperatures (Burkhard, 1993), has been plastically deformed (Fig. 5g and h). Neither reaction softening within the fault nor wall rock alteration is observed and detailed geochemical profiling has therefore not been carried out.

3.3. PT estimates

In order to constrain the metamorphic conditions during formation of the mineralized shear zones, temperatures were estimated from the rheological behavior of quartz and pressures were estimated using fluid inclusions. Oriented quartz samples were collected from discordant quartz–carbonate–sulphide veins and boudin necks (Figs. 3a and 6) that represent the latest stage of semi-ductile deformation (west–east stretch) and ore deposition. Quartz shows evidence for dislocation climb regime. This constrains mylonitisation and veining to a temperature range 350–400 °C, using empirical and experimental calibrations (Christie and Ord, 1980; Hirth and Tullis, 1992; Okudaira et al., 1995). This is consistent with the chlorite–muscovite bearing mineral assemblage of the surrounding quartz phyllites and within errors expected for average *PT* estimates based on mineral compositions at this metamorphic grade (Cartwright and Buick, 1999).

Fluid inclusions in Type-I structures appear on planes (trails in two-dimensional sections) oriented approximately perpendicular to the general direction of stretch (Fig. 6a). They fit an west–east extensional stress field and are therefore likely to have formed synchronously with veining and ore precipitation (Figs. 2 and 6). All analyzed fluid inclusions are aqueous and range in size from 3 to 20 μm (for analytical details, see Fig. 6). No carbonic phases

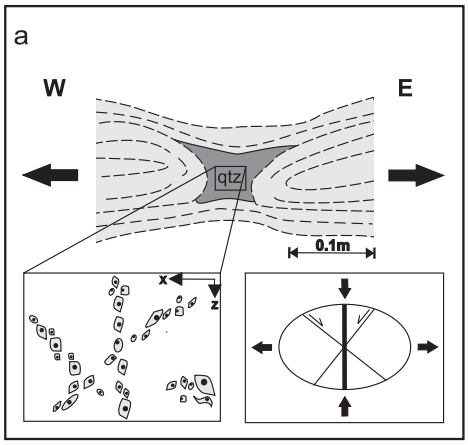

b Features of FI	
Number of FI	n=69
Size	3 to 20 μm
Number of phases at room temperature	2 / L+V
$Tm_{(H2O)}$ (°C)	-23°C to -18°C, (-14°C)
wt.% NaCl (equivalent)	21,6% to 23%, (16,9%)
density (g/cm^3)	1,055 to 1,087 (1,029)
Th (°C)	155°C to 175°C, (190°C)
Behaviour of homogenisation	L+V → L
Te (°C)	-35°C to -40°C, (-62°C)
Chemical system	NaCl-H_2O, NaCl-$CaCl_2$-H_2O

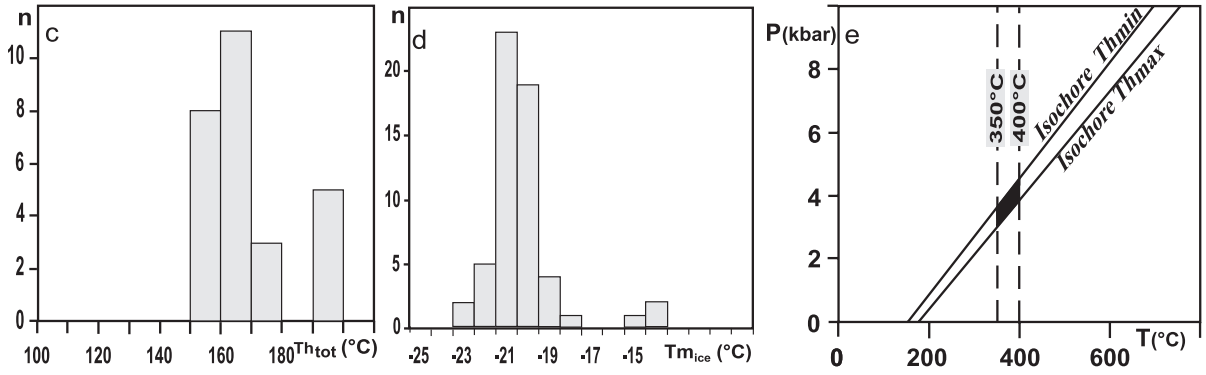

Fig. 6. Fluid inclusions. Microthermometry on fluid inclusions was performed on a Chaixmeca heating–freezing stage mounted onto an Olympus BH-2 transmitted light microscope. The standard instrument was improved by: (1) An Omega CN 3000 Thermo-Controller; (2) Video equipment including a Panasonic CCTV-WV-BL600/G black and white video camera; (3) A NFK 6.7 × ND 125 projective and an IC 80 long-distance objective ULWD MSPLAN 80 $-0.75^{\infty}/0$ $f=180$ and (4) A Panasonic black and white video monitor WV-BM1400. Fluid inclusions were studied on double-polished wafers, about 150 μm thick. Quartz was the host mineral of all the fluid inclusions measured. Densities, salinities and isochores were calculated using the Computer Code Flincor 1.4 (Brown, 1989) and the formula of Brown and Lamb (1989). (a) The schematic sketch shows sampled quartz veins from boudin necks (compare with Fig. 3), the orientation of the fluid inclusion trails and inferred paleo-stress regime at the time of veining (insets). (b) Details of fluid inclusion analyses. Te, Tm and Th stand for temperatures of first melting, total melting and total homogenization, respectively. L and V stand for liquid phase and vapour phase. Values in brackets are individual outliers. (c) Final melt temperatures of ice (Tm) and (d) temperatures of total homogenization (Th_{tot}). n = number of measured inclusions. (e) Isochores calculated using maximum and minimum homogenization temperatures(Th_{max}, Th_{min}). The temperature range was estimated by the rheological behavior of quartz and mineral assemblages developed synchronous to the veining.

(CO_2) were observed. The degree of fill varies between 0.85 and 0.95. At room temperature all fluid inclusions are biphase, containing a liquid and a vapor phase. Morphologically, the fluid inclusions show a wide range of shapes including amoeboidal, ovoidal, spheroidal and negative crystal forms. Most total homogenization temperatures (Th_{tot}) vary between 150 and 180 °C (Fig. 6b and c) with homogenization into the liquid phase. Densities of fluid inclusions are between 1.055 and 1.087 g/cm^3. Higher values of Th_{tot} (not considered for calculation of isochors) are found to be artefacts caused by leakage of large fluid inclusions as recognized by repeated heating–freezing experiments (Fig. 6b). A range of isochors (Fig. 6d) was calculated using minimum and maximum Th_{tot} values. From the isochors and the temperature estimates of 350–400 °C, a pressure range of 3.5–4.5 kbar was calculated (Fig. 6d).

Final melting of ice (Tm) occurs in a temperature range between −23 and −18 °C (Fig. 6c). This corresponds to a very high salinity between 21 and 23 wt.% NaCl equivalent. This type of saline fluid that was also observed from other Cretaceous metamorphic ore occurrences (Pohl and Belocky, 1999) is suitable to transport metals as Cl-complexes. Salinity, orientation and *PT* estimates are consistent with the physical conditions and stress regime during Cretaceous Eoalpine metamorphism as reported by Thöni (1999), Neubauer et al. (1995) and others.

4. Analytical techniques

Major and selected trace elements of bulk rock samples were measured by X-ray fluorescence analysis (XRF) with a Philips PW1404 wavelength-dispersive X-ray spectrometer at the Institute of Applied Mineralogy, Technical University of Graz and by ACTLABS in Canada. Glass discs were used for major elements, pressed powder pellets for trace elements. Calibration was done with 21 international geochemical reference samples. Precision and accuracy was monitored by repeated measurement of the reference materials GSP-2, G-2, W-2 and DNC-1. The reproducibility was found to be smaller than 1% for major elements and smaller than 2% for trace elements.

Rare earth elements (REE) and trace elements were analyzed by ICPMS at the Institute of Mineralogy and Petrology and the Institute of Chemistry, University of Graz. Finely powdered whole rock samples (0.1 g) were digested with 0.2 ml HF and 5 ml HNO_3 in Teflon bombs at 200 °C for 24 h and diluted to 100 ml. Every 5 samples the Open University standard OU4 was solubilized and analyzed and was found to be within 15% of the recommended value. Standard solutions for REE were prepared from a Alfa Aesar 100 ppm REE multi-element standard solution. Reproducibility is smaller than 1%.

5. Geochemical changes in Type-I structures

In order to obtain information on mass transfer across the shear zone, whole rock geochemistry was obtained from a suite of samples collected across the Crombach shear zone. The samples were collected from the protolith, from subzone-A and subzone-B on the south side of the shear zone center (subzone-B_S), from the shear zone center (subzone-C) and from subzone-B north of the shear zone center (subzone-B_N). Subzone-A north of the shear zone center could not be sampled because of lacking outcrop. In order to reduce the influence of inhomogeneities caused by ore bodies in subzone-B and subzone-C, samples were collected carefully excluding quartz and carbonate veins. As a consequence, gain of Si, Ca, Mg, Mn and Fe in the center of the shear zone (subzone-C) represent only minimum values.

Each of the subzones show unique chemical characteristics. Fig. 7 shows these trends normalized to the element concentration of the protolith (the undeformed granodiorite). The protolith was defined by the average composition of five samples collected arbitrarily distributed over several hundreds of meters (Table 1). It may be seen that the standard deviation for most major elements is typically below 0.3%, indicating little compositional variation within the granodiorite.

The concentration changes of Si, Al, Ti and Zr are shown in Fig. 7a. Al. Ti and Zr are often considered as immobile elements in the literature (Goddard and Evans, 1995; Yang et al., 1998; Zulauf et al., 1999) although we note that Ti mobility was demonstrated by Selverstone et al. (1991) elsewhere in the Eastern Alps. It may be seen that these three elements behave very similar. They are enriched in subzone-B and depleted in subzone-C, relative to the protolith. By contrast, Si which is mobile in many geological settings is enriched in subzone-C. Note that because of the normalisation to the protolith, even a small enrichment factor in Fig. 7 implies the transfer of several weight percent for abundant elements as Si. The behavior of the immobile elements Al, Ti and Zr is confirmed by the distribution of the rare earth elements. Both the light rare earth's (Fig. 7b) and the heavy rare earth's (Fig. 7c) largely confirm the trends shown by Al, Ti and Zr.

The concentration changes of Na, K, Rb, Sr and Ba are shown in Fig. 7d. These are the elements that best reflect the behavior of feldspar. The gradual disappearance of the magmatic plagioclase is best documented by the massive loss of Sr and Ba across all subzones. Final breakdown of albite caused a major

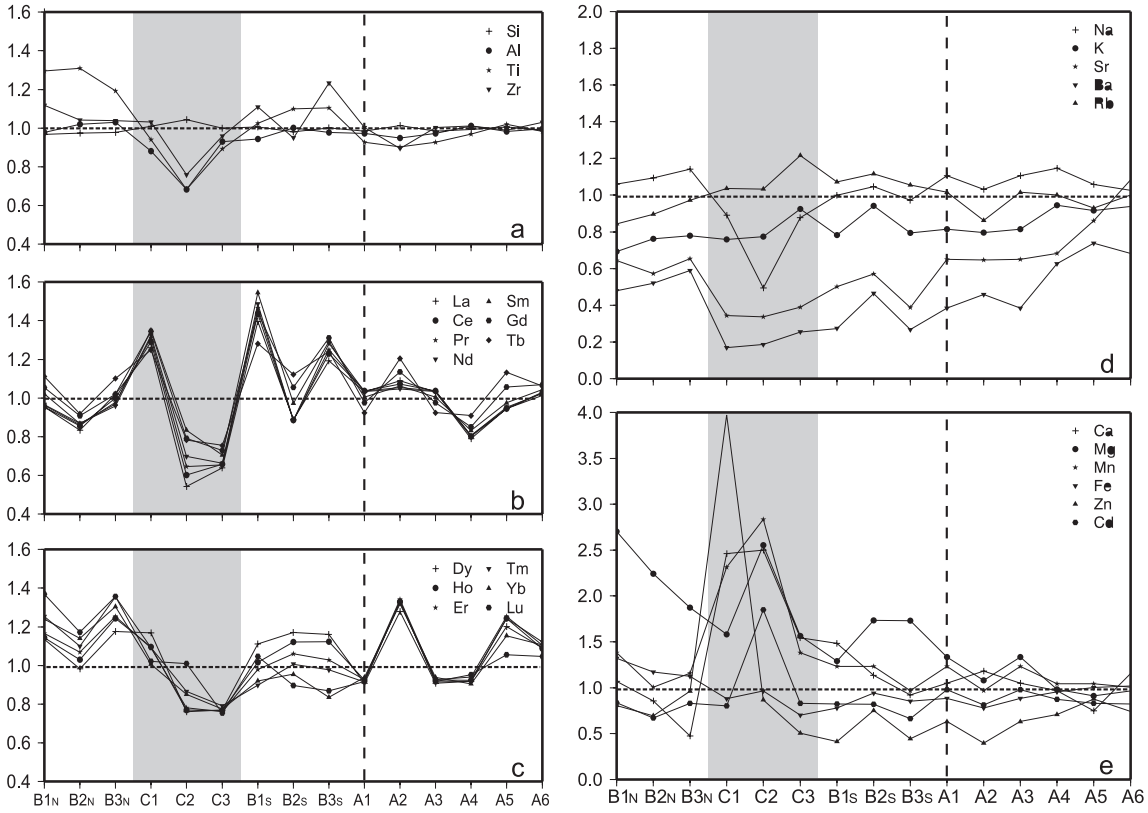

Fig. 7. Concentration of major and selected trace elements across the subzone-A, subzone-B and subzone-C of the Crombach shear zone normalized against the protolith. (a) Enrichment/depletion trends of the "immobiles" and the highly mobile Si. (b) Trends of light rare earth elements. (c) Heavy rare earth elements. (d) Elements compiled in this plot reflect the breakdown process of feldspars. (e) External fluid and precipitation of carbonates and sulphides is responsible for the extreme enrichment of Ca, Mg and Mn. Gray shading shows subzone-C, the dashed vertical line the boundary between subzone-A and subzone-B.

relative reduction in Na in subzone-C. The disappearance of K-feldspar had minor geochemical impact. The released K remained in the system to form sericite. K is partly removed from subzone-A and subzone-B by breakdown of K-feldspar. Rb behaves in a similar way to K because it is also released by the K-feldspar breakdown and is incorporated in mica.

Element distributions of the remaining major elements of interest are shown in Fig. 7e. Cd and Zn are shown in Fig. 7e because they also reflect the strong enrichment of metallic elements in the shear zone center. Ca shows a spectacular enrichment in the shear zone center. This is in contrast to the observation that plagioclase disappears towards the center of the shear zone and must be related to microscopic carbonate veins. This is confirmed with the enrichment of Mg and Mn. While the breakdown of plagioclase and K-feldspar control the chemical changes of the outer parts of the shear zone, the loss of Ca is overcompensated by carbonate precipitation processes from an external source (compare Figs. 4 and 5). This is confirmed by the trends of Cd and Zn and also shown by Cu which has a 60-fold enrichment (see Table 1; not shown in Fig. 7e). Despite of that, there is no Sr enrichment at the center of the shear zone (Fig. 7d). This might indicate that the breakdown of plagioclase and the deposition of the carbonates reflect two independent processes caused by two different fluids. Fe shows only minor variation throughout the shear zone, but its variation is not representative as veins and sulphides were not sampled. In summary, the concentration changes of the elements shown in Fig.

7c cannot be explained with mass transfer between different parts of the shear zone and must be explained by an external source.

5.1. Mass transfer across Type-I structures

The relative abundance of elements in the altered rocks and the protolith gives only an idea about the depletion or enrichment of elements relative to the protolith. It does not show the absolute gain and loss of mobile elements frequently associated with volume changes. Such volume changes are observed in numerous shear zones (Selverstone et al., 1991; Goddard and Evans, 1995; Hippertt, 1998; Bialek, 1999) and may be used to infer the addition and or extraction of mass from the shear zone. In general, two end-

Table 1
Whole rock geochemical data from a profile across the Crombach shear zone (see Fig. 1)

		Subzone B(north)					Subzone C					Subzone B(south)				
		B1N	B2 N	B3 N	μ B N	1 σ BN	C1	C2	C3	μ C	1 σ C	B1s	B2s	B2s	μ Bs	1 σ Bs
SiO2	%	69.86	70.30	70.55	70.24	0.35	72.91	75.32	72.14	73.46	1.66	72.59	70.81	72.21	71.87	0.94
Al2O3	%	14.96	15.62	15.78	15.45	0.43	13.49	10.45	14.24	12.73	2.01	14.46	15.32	14.98	14.92	0.43
Fe2O3	%	2.02	1.79	1.72	1.84	0.16	1.35	1.48	1.07	1.30	0.21	1.19	1.44	1.30	1.31	0.13
MnO	%	0.04	0.03	0.03	0.03	0.01	0.06	0.08	0.04	0.06	0.02	0.03	0.03	0.03	0.03	0.00
MgO	%	1.76	1.46	1.22	1.48	0.27	1.03	1.66	1.02	1.24	0.37	0.84	1.13	1.13	1.03	0.17
CaO	%	1.04	0.83	0.46	0.78	0.29	2.39	2.43	1.50	2.11	0.52	1.44	1.10	0.90	1.15	0.28
Na2O	%	5.05	5.21	5.44	5.23	0.20	4.25	2.36	4.18	3.60	1.07	4.76	4.99	4.63	4.79	0.18
K2O	%	2.00	2.20	2.25	2.15	0.13	2.19	2.23	2.67	2.37	0.26	2.26	2.72	2.30	2.43	0.26
TiO2	%	0.28	0.28	0.26	0.27	0.01	0.20	0.15	0.19	0.18	0.03	0.22	0.24	0.24	0.23	0.01
P2O5	%	0.09	0.09	0.09	0.09	0.00	0.06	0.05	0.09	0.07	0.02	0.06	0.10	0.09	0.08	0.02
LOI	%	2.11	2.09	1.53	1.91	0.33	2.21	3.21	2.59	2.67	0.50	2.27	1.98	2.14	2.13	0.15
TOTAL	%	99.20	99.90	99.33	99.48	0.37	100.14	99.42	99.73	99.76	0.36	100.12	99.86	99.94	99.97	0.14
Rb	(ppm)	59.0	62.6	68.0	63.20	4.53	72.5	72.2	85.0	76.57	7.31	75.0	78.0	73.8	75.60	2.16
Sr	(ppm)	205.3	182.3	208.4	198.66	14.25	109.6	107.2	124.0	113.60	9.09	159.6	181.9	123.7	155.07	29.38
Zr	(ppm)	126.0	117.4	117.0	120.13	5.08	116.2	85.6	108.0	103.27	15.84	125.0	107.0	139.0	123.67	16.04
51 V	(ppm)	23.6	24.2	20.4	22.70	2.06	8.5	17.0	13.1	12.88	4.28	10.5	18.3	13.3	14.00	3.95
52 Cr	(ppm)	17.2	18.7	12.9	16.25	3.02	4.6	2.9	9.8	5.77	3.57	3.8	12.5	6.9	7.73	4.41
59 Co	(ppm)	3.7	74.6	4.1	27.49	40.83	113.5	62.9	1.3	59.24	56.20	1.2	2.4	53.8	19.13	30.05
60 Ni	(ppm)	9.8	8.9	6.7	8.43	1.60	4.4	4.5	4.1	4.30	0.23	2.0	6.5	3.9	4.12	2.29
65 Cu	(ppm)	1.8	4.4	3.1	3.10	1.32	12.0	281.3	2.6	98.60	158.27	2.0	4.1	2.5	2.87	1.13
66 Zn	(ppm)	32.7	28.1	39.0	33.28	5.49	161.0	35.2	20.5	72.21	77.23	16.7	30.5	18.0	21.76	7.60
93 Nb	(ppm)	3.0	2.3	3.9	3.09	0.77	1.1	1.6	1.6	1.42	0.28	1.0	1.7	0.6	1.10	0.57
111 Cd	(ppm)	0.1	0.0	0.1	0.06	0.01	0.1	0.1	0.1	0.08	0.04	0.1	0.1	0.0	0.05	0.01
137 Ba	(ppm)	611.6	663.6	750.9	675.36	70.36	216.1	237.3	324.6	259.31	57.49	348.4	592.4	340.5	427.12	143.23
139 La	(ppm)	15.3	13.4	16.4	15.01	1.52	20.2	8.7	10.2	13.05	6.25	22.4	14.3	19.1	18.59	4.10
140 Ce	(ppm)	32.5	29.2	34.1	31.92	2.48	44.0	20.5	22.4	28.96	13.07	48.9	30.2	41.9	40.36	9.46
141 Pr	(ppm)	3.9	3.5	4.0	3.79	0.26	5.3	2.6	2.7	3.54	1.55	6.0	3.6	5.1	4.88	1.19
146 Nd	(ppm)	14.5	13.0	14.4	13.95	0.80	19.8	10.4	9.9	13.39	5.57	22.3	13.3	19.2	18.24	4.58
147 Sm	(ppm)	3.0	2.5	2.8	2.79	0.23	4.0	2.4	2.1	2.82	1.00	4.5	2.8	3.8	3.72	0.84
153 Eu	(ppm)	0.9	0.9	0.9	0.88	0.04	0.8	0.6	0.6	0.67	0.14	1.0	0.8	0.8	0.86	0.09
157 Gd	(ppm)	2.5	2.2	2.4	2.37	0.18	3.2	1.9	1.7	2.28	0.81	3.4	2.5	3.1	3.03	0.47
159 Tb	(ppm)	0.3	0.3	0.3	0.32	0.03	0.4	0.2	0.2	0.29	0.09	0.4	0.3	0.4	0.38	0.03
163 Dy	(ppm)	1.7	1.5	1.8	1.69	0.16	1.8	1.2	1.2	1.38	0.36	1.7	1.8	1.8	1.77	0.05
165 Ho	(ppm)	0.3	0.3	0.3	0.30	0.03	0.3	0.2	0.2	0.24	0.05	0.3	0.3	0.3	0.29	0.02
166 Er	(ppm)	0.8	0.7	0.9	0.81	0.06	0.8	0.5	0.5	0.61	0.13	0.7	0.7	0.7	0.71	0.03
169 Tm	(ppm)	0.1	0.1	0.1	0.11	0.01	0.1	0.1	0.1	0.08	0.01	0.1	0.1	0.1	0.08	0.00
172 Yb	(ppm)	0.6	0.6	0.7	0.64	0.04	0.5	0.4	0.4	0.45	0.06	0.5	0.5	0.4	0.47	0.03
175 Lu	(ppm)	0.1	0.1	0.1	0.08	0.01	0.1	0.1	0.0	0.06	0.01	0.1	0.1	0.1	0.06	0.01
205 Tl	(ppm)	0.2	0.3	0.3	0.28	0.04	0.3	0.4	0.4	0.36	0.02	0.3	0.4	0.3	0.34	0.03
232 Th	(ppm)	4.4	3.8	3.0	3.71	0.71	7.2	3.7	3.2	4.74	2.17	7.5	8.2	7.9	7.88	0.37
238 U	(ppm)	1.8	2.0	1.3	1.68	0.37	0.7	1.9	0.9	1.18	0.64	1.8	1.5	1.0	1.42	0.41

(continued on next page)

Table 1 (*continued*)

		Subzone A								Protolith						
		A1	A2	A3	A4	A5	A6	μ A	1 σ A	P1	P2	P3	P4	P5	μ P	1 σ P
SiO2	%	70.98	73.10	71.12	71.58	72.57	71.21	71.76	0.87	71.86	72.17	71.95	72.76	72.09	72.16	0.35
Al2O3	%	14.90	14.53	14.94	15.50	15.04	15.25	15.03	0.33	15.49	15.42	15.43	15.17	15.06	15.31	0.19
Fe2O3	%	1.35	1.19	1.46	1.46	1.54	1.56	1.43	0.14	1.51	1.54	1.68	1.65	1.27	1.53	0.16
MnO	%	0.03	0.03	0.05	0.03	0.03	0.03	0.03	0.01	0.02	0.02	0.03	0.03	0.03	0.03	0.00
MgO	%	0.87	0.71	0.92	0.64	0.59	0.63	0.73	0.14	0.66	0.65	0.81	0.72	0.42	0.65	0.14
CaO	%	1.02	1.15	2.15	0.94	0.73	1.12	1.18	0.50	1.14	0.86	0.68	0.60	1.57	0.97	0.39
Na2O	%	5.27	4.92	4.85	5.46	5.04	4.89	5.07	0.24	4.64	4.94	4.92	4.81	4.51	4.77	0.18
K2O	%	2.35	2.30	2.52	2.73	2.65	2.71	2.54	0.19	2.90	2.63	2.83	2.61	3.47	2.89	0.35
TiO2	%	0.20	0.19	0.20	0.21	0.22	0.21	0.21	0.01	0.22	0.22	0.22	0.23	0.18	0.21	0.02
P2O5	%	0.09	0.06	0.08	0.08	0.06	0.08	0.07	0.01	0.06	0.06	0.12	0.07	0.07	0.07	0.03
LOI	%	1.73	1.87	1.91	1.32	1.73	1.31	1.65	0.27	1.67	1.76	1.23	1.59	0.88	1.43	0.37
TOTAL	%	98.79	100.03	100.19	99.95	100.17	99.00	99.69	0.63	100.18	100.26	99.90	100.24	99.55	100.03	0.30
Rb	(ppm)	71.0	60.3	71.8	70.0	65.0	70.0	68.02	4.47	65.6	69.6	81.0	70.4	63.0	69.92	6.89
Sr	(ppm)	207.3	206.2	257.9	217.5	274.2	345.6	251.46	53.97	361.4	295.9	191.1	174.9	571.2	318.90	160.52
Zr	(ppm)	113.0	100.9	108.2	114.0	111.6	116.0	110.62	5.43	110.9	113.3	119.0	111.4	109.0	112.72	3.83
51 V	(ppm)	12.4	10.6	11.5	13.0	16.2	13.7	12.91	1.94	16.0	12.9	14.7	13.2	11.1	13.58	1.88
52 Cr	(ppm)	5.7	3.9	4.8	3.7	4.4	3.7	4.36	0.79	5.1	4.1	4.1	5.1	3.9	4.44	0.58
59 Co	(ppm)	1.9	28.8	15.3	2.0	38.0	1.8	14.63	15.71	103.2	37.4	2.9	52.2	1.4	39.41	41.88
60 Ni	(ppm)	2.9	2.0	2.5	1.8	2.6	2.1	2.32	0.42	3.1	2.2	2.8	3.0	3.1	2.83	0.36
65 Cu	(ppm)	3.8	3.4	3.6	3.2	11.0	1.6	4.43	3.32	5.8	4.4	5.2	2.8	3.3	4.29	1.27
66 Zn	(ppm)	25.6	16.0	20.8	28.7	35.5	30.0	26.13	6.94	31.4	34.6	39.4	31.4	65.9	40.54	14.57
93 Nb	(ppm)	3.5	3.6	3.6	3.9	4.7	4.1	3.89	0.44	101.3	4.1	4.2	3.6	3.5	23.34	43.58
111 Cd	(ppm)	0.1	0.1	0.1	0.1	0.1	0.1	0.06	0.00	0.1	0.0	0.1	0.1	0.1	0.07	0.03
137 Ba	(ppm)	489.5	584.3	536.9	798.1	940.4	870.0	703.22	190.03	1021.0	982.6	930.2	822.0	2620.1	1275.17	755.54
139 La	(ppm)	16.5	17.5	17.0	12.7	15.2	16.3	15.85	1.74	14.6	14.5	19.1	15.7	16.3	16.04	1.89
140 Ce	(ppm)	35.4	36.5	35.9	27.3	32.2	35.0	33.73	3.47	31.2	31.0	40.5	33.5	34.3	34.09	3.87
141 Pr	(ppm)	4.2	4.3	4.2	3.3	3.8	4.2	4.01	0.39	3.7	3.7	4.8	4.0	4.1	4.07	0.43
146 Nd	(ppm)	15.5	15.7	15.6	12.0	14.3	15.3	14.73	1.41	14.0	13.6	17.3	14.7	15.2	14.98	1.46
147 Sm	(ppm)	2.9	3.1	3.0	2.4	2.9	3.1	2.91	0.25	2.9	2.6	3.3	2.9	3.0	2.93	0.23
153 Eu	(ppm)	0.7	0.8	0.8	0.8	0.9	0.9	0.83	0.08	0.9	0.8	0.9	0.8	1.1	0.90	0.14
157 Gd	(ppm)	2.3	2.7	2.5	2.0	2.5	2.6	2.44	0.24	2.5	2.1	2.6	2.3	2.4	2.39	0.18
159 Tb	(ppm)	0.3	0.4	0.3	0.3	0.4	0.3	0.33	0.04	0.3	0.3	0.3	0.3	0.3	0.31	0.03
163 Dy	(ppm)	1.4	2.0	1.7	1.4	1.8	1.7	1.67	0.23	1.8	1.4	1.6	1.4	1.5	1.54	0.16
165 Ho	(ppm)	0.2	0.4	0.3	0.2	0.3	0.3	0.30	0.04	0.3	0.2	0.3	0.2	0.3	0.27	0.03
166 Er	(ppm)	0.6	0.9	0.8	0.7	0.9	0.8	0.78	0.11	0.8	0.6	0.7	0.6	0.7	0.69	0.07
169 Tm	(ppm)	0.1	0.1	0.1	0.1	0.1	0.1	0.10	0.01	0.1	0.1	0.1	0.1	0.1	0.09	0.01
172 Yb	(ppm)	0.5	0.7	0.6	0.5	0.6	0.6	0.56	0.08	0.6	0.5	0.5	0.5	0.5	0.52	0.05
175 Lu	(ppm)	0.1	0.1	0.1	0.1	0.1	0.1	0.07	0.01	0.1	0.1	0.1	0.1	0.1	0.06	0.01
205 Tl	(ppm)	0.4	0.3	0.3	0.3	0.4	0.3	0.34	0.02	0.4	0.4	0.4	0.3	0.3	0.38	0.04
232 Th	(ppm)	4.8	5.4	5.1	2.8	3.8	4.4	4.39	0.98	3.7	3.9	4.2	3.8	4.2	3.98	0.24
238 U	(ppm)	1.8	4.7	3.3	2.7	1.2	2.6	2.72	1.21	1.6	1.9	5.3	1.5	1.7	2.39	1.62

Samples P1 to P5 are from the protolith; samples A1 to A6 are from subzone-A; samples $B1_N$ to $B3_N$ are from the northern part of subzone-B; samples C1 to C3 are from subzone-C; samples $B1_S$ to $B3_S$ are from the southern part of subzone-C. Mean (μ) and 1 sigma (σ) errors are shaded in gray.

member scenarios of mass transfer may be distinguished. These are: (1) mass transfer between subzones (closed chemical system for the whole shear zone) and (2) transfer of mass from an external source (open chemical system). Both end-members cause mass changes within single subzones, but only the

Fig. 8. Isocon plots. Plots of element concentration in the protolith (horizontal axes) versus the concentration in the deformed and altered rocks of the different subzones (vertical axes). Axes are plotted logarithmically and errors are 1 sigma errors from averaged analyses as shown in Table 1. For each subzone, two diagrams are shown with different concentration ranges. The isocon on each diagram pair is the same best fit isocon for selected elements assumed as immobile as calculated with the approach discussed in the text. "A" is for subzone-A; "B_N" and "B_S" for subzone-B north of the shear zone and subzone-B south of the shear zone and "C" is for the subzone-C.

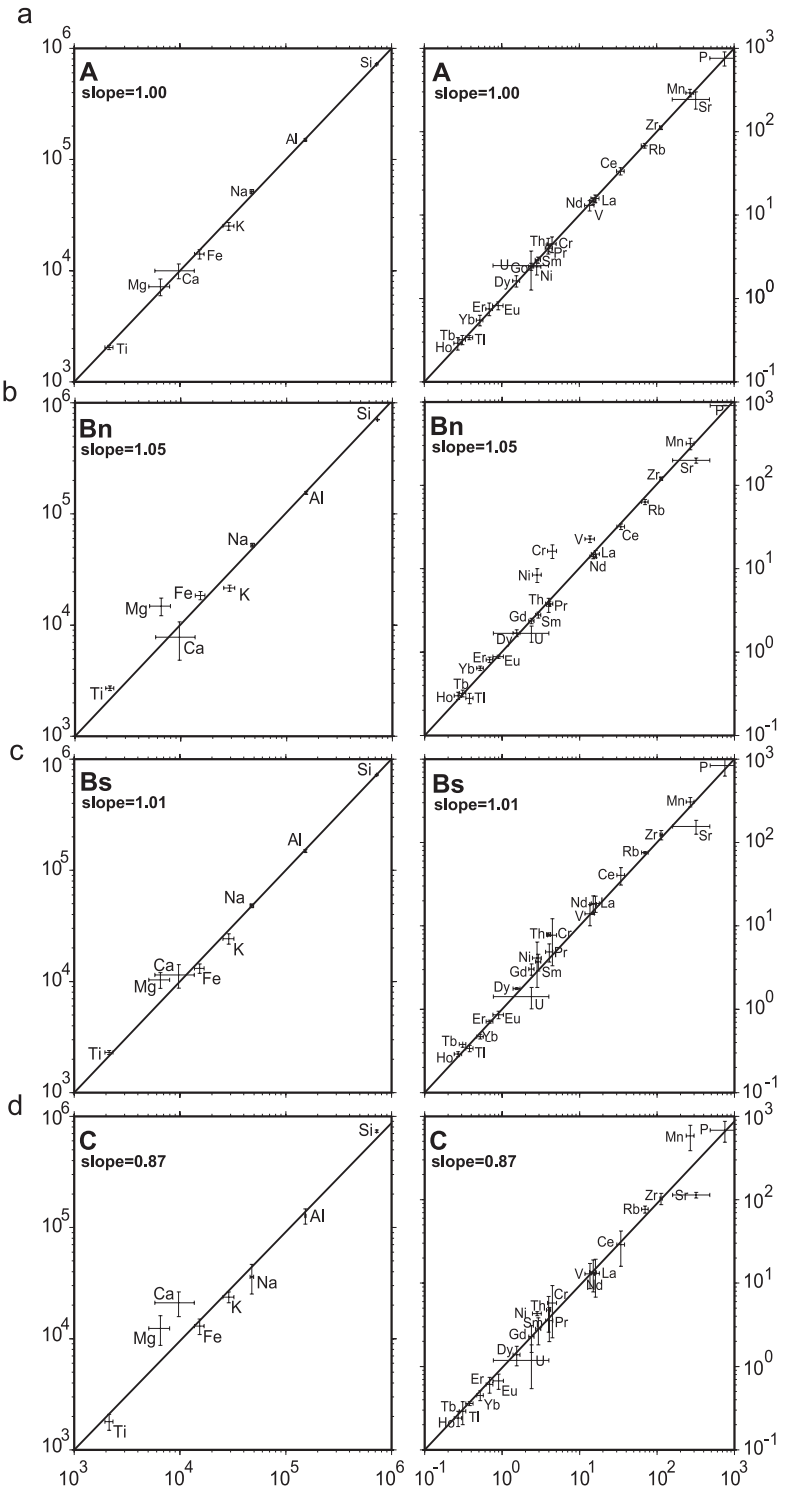
a
A
slope=1.00
Si
Al
Na
K
Fe
Ca
Mg
Ti
A
slope=1.00
P
Mn
Sr
Zr
Rb
Ce
Nd
La
V
Th
Cr
Pr
U
Gd
Sm
Dy
Ni
Er
Eu
Yb
Tb
Ho
Tl
b
Bn
slope=1.05
Si
Al
Na
Fe
K
Mg
Ca
Ti
Bn
slope=1.05
P
Mn
Sr
Zr
Rb
Ce
V
La
Cr
Nd
Ni
Th
Pr
Gd
Sm
Dy
U
Er
Eu
Yb
Tb
Ho
Tl
c
Bs
slope=1.01
Si
Al
Na
K
Ca
Mg
Fe
Ti
Bs
slope=1.01
P
Mn
Zr
Sr
Rb
Ce
Nd
La
V
Th
Cr
Ni
Pr
Gd
Sm
Dy
U
Er
Eu
Yb
Tb
Ho
Tl
d
C
slope=0.87
Si
Al
Ca
Na
K
Mg
Fe
Ti
C
slope=0.87
Mn
P
Zr
Sr
Rb
Ce
V
La
Nd
Cr
Th
Ni
Sm
Pr
Gd
Dy
U
Er
Eu
Yb
Tb
Ho
Tl

open system scenario can cause an overall mass change. Both scenarios and the immobility of elements during mass gain or loss can be described graphically on an isocon plot (Grant, 1986). In the isocon plot, the element concentrations of the protolith (the least altered rock) are plotted against the element concentrations of the altered rocks (samples from the subzone-A, subzone-B and subzone-C). An "isocon" is a line of constant mass on this diagram. Immobile elements plot on a straight line passing through the origin of the diagram (Fig. 8) in all domains of the shear zone. The slope of this line need not to be 1. A shallower or steeper slope indicates dilution or concentration of immobile elements in the altered rock relatively to the protolith.

Isocon plots for the three different subzones of the investigated shear zone are shown in Fig. 8. These diagrams are refined from a "normal" isocon plot (Grant, 1986) by using a logarithmic scale, proper error bars for each element and a least square approach for fitting isocons (Baumgartner and Olsen, 1995). Note that because of the logarithmic scale the error bars appear asymmetric. The error bars are 1 standard deviation from the mean over all samples from each subzone (Table 1). For better clarity, the same isocon for each subzone is shown on two diagrams with different scales for different elements.

In subzone-A, there is little mass transfer (Fig. 8a). Practically all analyzed elements lie on an isocon with the slope of 1. Only Sr deviates slightly from this line which is easily explained by the initial breakdown of plagioclase. It may be concluded that the shear zone margins (subzone-A) have mainly been deformed under conditions of nearly constant mass and volume.

The isocon plot for subzone-B is shown in Fig. 8b and c (B_N and B_S for north and south, respectively). Most elements still lie on a line through the origin with a best fit slope for the northern subzone-B_N of 1.05, indicating roughly 5% mass loss from the subzone. The best isoscon fit for the southern subzone-B has a slope of 1.01, indicating only 1% mass loss. Note that the mass loss is roughly equivalent to the volume loss as the density differences between minerals are relatively small. The most significant departure from the isocon is given by K and Sr that show a significant depletion in subzone-B on both sides of the shear zone center. This is due to the feldspar breakdown in subzone-B and the removal of the breakdown products from the subzone. This is confirmed by some removal of Ca and Sr from subzone-B (volume loss). Mg shows a major enrichment in both the northern and the southern subzone-B. However, Ca is only enriched in the southern subzone-B_S, but depleted in the northern subzone-B_N. This apparently contrasting trend can be explained by variable carbonate addition in the two parts of subzone-B: The Mg content of the protolith is small as usually observed in felsic magmatic rocks. Even small amounts of Mg from an external source would result in significant enrichment relative to the protolith. The same amount of Ca from an external source would never compensate the loss of Ca caused by the breakdown of magmatic plagioclase. Therefore, a minor addition of carbonate will always reflect an enrichment of Mg, but may cause enrichment or depletion of Ca at the same time.

An isocon plot for the center of the shear zone (subzone-C) is shown in Fig. 8d. A best fit for the immobile elements defines an isocon with a slope of 0.87. This indicates net mass transport of the order of 13% and therefore massive volume gain in the shear zone center. Note that this result is derived from mean analyses. Individual samples from the shear zone center show significantly higher enrichments (Table 1). Na, K, Fe and Sr are depleted relative to the protolith. Na is released during the albite to sericite reaction and removed from the shear zone. The same applies for Sr through the albitisation of plagioclase. All other elements show either a consistent mass or a mass gain. Carbonates from an external source are considered responsible for the extraordinary gain of Mg, Ca and Mn, corresponding to the enrichment of Si in the quartz veins. However, since Si is the most abundant element even a small enrichment factor results in a gain of mass. In addition, gain of Si, Ca, Mg and Mn represents minimum values since abundant veins from subzone-C had been excluded from sampling.

6. Interpretation of the fluid source

6.1. Fluids in Type-I structures

The observed mineralogical changes provide information on the fluid regime. In Type-I structures, the

observed breakdown reactions are well known from many shear zones around the world to be related to an acidic fluid (e.g. Piessens et al., 2002). For example, O'Hara (1988) and Hippertt (1998) have interpreted the breakdown of feldspar to epidote, here observed in subzone-A, to follow the reaction:

$$Na_4CaAl_6Si_{14}O_{40} + 1.5KAlSi_3O_8 + 0.5K^+ + 0.5H_2O + 3.5H^+ = 0.5Ca_2Al_3Si_3O_{12}(OH) + 2KAl_3Si_3O_{10}(OH)_2 + 11SiO_2 + 4Na^+ \quad (1)$$

Similarly, the breakdown of feldspar to sericite observed in subzone-B also requires an acidic fluid. Equivalent observations in North Carolina and the Western Alps have been interpreted by Wibberly (1999) and Newman and Mitra (1993), respectively, to be the consequence of the reaction:

$$3KAlSi_3O_8 + 2H^+ = KAl_3Si_3O_{10}(OH)_2 + 6SiO_2 + 2K^+ \quad (2)$$

Finally, the breakdown of albite with any remaining feldspar to sericite observed here predominantly in subzone-C has been interpreted by Newman and Mitra (1993) to follow the reaction:

$$2NaAlSi_3O_8 + KAlSi_3O_8 + 2H^+ = KAl_3Si_3O_{10}(OH)_2 + 6SiO_2 + 2Na^+ \quad (3)$$

Note that all these reactions (a) require an acidic fluid, (b) produce the observed reaction products and (c) produce two additional components not yet discussed. These include (i) Si and (ii) free cations of K^+ and Na^+. Considering that Si is depleted in subzone-B and abundant quartz veining plus Si enrichment is observed in subzone-C, lateral mass transfer of Si from subzone-B towards the shear zone center (subzone-C) is inferred.

The Na^+cations liberated by reactions (1) and (3) are easily accounted for by the observed albitisation in all subzones. Such albitisation of K-feldspar is well described by the reaction:

$$KAlSi_3O_8 + Na^+ = NaAlSi_3O_8 + K^+ \quad (4)$$

This reaction is not only associated with the consumption of Na^+, but also with a decrease in volume (Hippertt, 1998) which corresponds well with the observation that this reaction is mainly observed in areas of stress concentration (see above). Finally, the potassium released by reactions (2) and (4) may be consumed in the further breakdown of albite according to the reaction:

$$3NaAlSi_3O_8 + K^+ + 2H^+ = KAl_3Si_3O_{10}(OH)_2 + 6SiO_2 + 3Na^+ \quad (5)$$

(Wibberly, 1999). This accounts well for the intense sericitisation of the shear zone center which is almost entirely composed of sericite and quartz. The coupled occurrence of reactions (1)–(5) is well recorded in the different subzones by the observed breakdown of feldspars (Fig. 5). Therefore, the fluids that infiltrated Type-I structures were most likely acidic fluids.

6.2. Fluids in Type-II structures

Feldspar to mica reactions in Type-I structures are controlled by an acidic fluid with a sufficient amount of free H^+. Such a fluid would rather dissolve carbonates than cause deposition. Hence, there must be a different fluid source that is responsible for the massive carbonate precipitation in the Type-II structures (and also to a minor extent in subzone-C of Type-I structures). We therefore interpret that a carbonate-bearing non-acidic fluid must have infiltrated these structures. Several arguments show that this fluid cannot have been related to the acidic fluids infiltrating Type-I structures: (a) The fluid inclusions measured in Type-I structures contain no CO_2. This has not only been observed in the investigated Crombach occurrence, but CO_2 is absent from fluid inclusions of most similar ore occurrences in the Eastern Alps (Pohl and Belocky, 1999). (b) The contrasting trend for Ca and Sr across the Type-I structures indicates that it is unlikely that Ca released by the breakdown of plagioclases was reprecipitated as carbonate in the shear zone center. If this was the case, the Sr that is also released during plagioclase breakdown would also have been reprecipitated in the carbonate. Summarizing the arguments, it is suggested that two different mechanisms, silicifica-

tion and carbonatisation, operated within the central shear zone portions.

7. Discussion

In this section an integrated interpretation of the ore-forming process is presented in terms of the observations. In summary these are: (i) Mineralogical observations in Type-I structures are largely consistent with infiltration by an external acidic fluid source. Acidic fluids typically enable transport of metals as chloride or sulphide complexes (Barnes and Seward, 1997; Reed, 1997; Liu et al., 2001; Müller and Seward, 2001). (ii) Mineralogical observations in Type-II structures indicate that these were infiltrated by a different external fluid precipitating carbonate. Such environments are known from classical ore traps (Reed, 1997; Seward and Barnes, 1997). (iii) Ore occurrences are linked to intersections of these two structures. Type-I and Type-II structures evolve coeval under the same stress regime (Fig. 2, see also below). The interaction of ductile shear zones and brittle faults is very likely to produce mesothermal ore deposits (Oliver, 2001). (iv) Textural and mineralogical observations in Type-I structures indicate that these formed in a series of successive stages in close interaction with Type-II structures. These observations include (a) the precipitation of carbonate within veins, (b) the opening of veins during progressive deformation and rotation in the direction to the foliation plane and (c) the formation of new, undeformed crosscutting carbonate-bearing veins. All these veins are mineralized at the dissolution contact with the carbonates (Fig. 5g and h).

These observations are best interpreted in terms of a cyclic fluid infiltration model with an alternating infiltration of acidic metal-bearing fluids (in Type-I structures) and CO_2-bearing fluids (from Type-II structures). Such a process is well known to be an ideal environment for ore formation (e.g. Seward and Barnes, 1997). H^+ cations in the acidic fluid react with $CaCO_3$ previously deposited by fluids from the Type-II structures. This process forms free H_2CO_3 and raises the pH value of the ore-bearing fluid. This in turn has the consequence that the ore-carrying complexes of the formerly acidic fluid become unstable (Fig. 5g and h). Precipitation is therefore linked to fluid neutralisation at the contact with carbonates, causing instability of metal-bearing complexes. This process is well documented by the precipitation of sulphide, albite and carbonate in the veins in Type-I and Type-II structures. However, observations especially in Type-I structures show that this coupled reaction was not a single phase process but must have occurred several times. A multiple infiltration process, as inferred here, can also explain the extremely high fluid–rock ratios required for an ore enrichment in the shear zones.

7.1. Cyclic fluid pumping during exhumation

We suggest that Cretaceous exhumation of the region provides the mechanism of cyclic opening and closure of the fluid pathways in a similar way to that suggested by Dugdale and Hagemann (2001). Our proposed mechanism involves several stages:

(i) Exhumation within a Cretaceous wrench corridor resulted in a decrease of lithostatic pressure at constant levels of pore fluid pressure. This leads to a fluid pressure controlled regime and ultimately in mechanic failure. Connected networks of fractures act as fluid conduits (Selverstone et al., 1991; Tourigny and Tremblay, 1997; Kisters et al., 2000) and allow the formation of large, open hydrothermal systems (Hippertt, 1998) including deep-seated shear zones (Type-I structures) and large-scale faults (Type-II structures). A pressure gradient between Type-I and Type-II structures is set up by the different permeability of ductile shear zones and open faults (Nguyen et al., 1998; Oliver, 2001). Such a fault valve behavior (Sibson et al., 1988) is convenient to channel fluids in shear zones and drain this fluid in faults. Mass transport over large distances is therefore enabled. Ore precipitates in Type-I and Type-II structures where an acidic metal-rich fluid gets in contact with carbonate.

(ii) Fluid migration and channeling in Type-I structures is associated with the progressive mineral alteration and mass transfer between different subzones (Fig. 9). Subzone-B is characterized by volume loss, while the shear

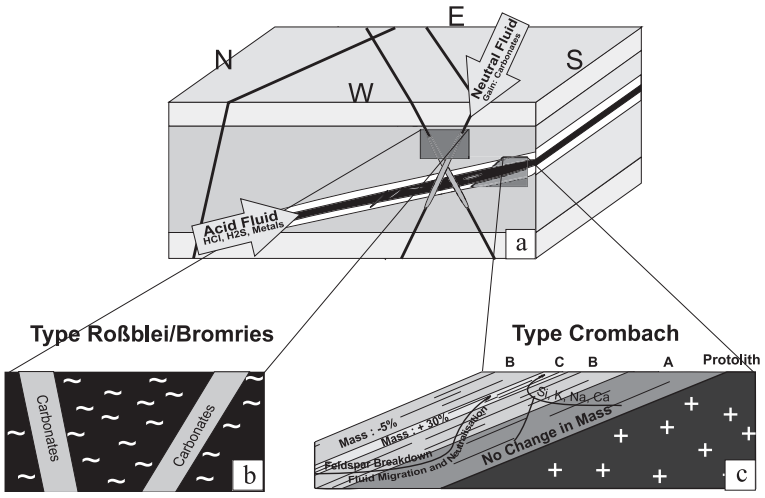

Fig. 9. Genetic model. (a) The block diagram illustrates the intersection of the two ore-bearing structures (Type-I, Type-II). The arrows indicate two different fluids migrating through the structures. (b) Position of ore occurrences of the type Rossblei–Bromries. (c) Position of ore occurrences of the type Crombach. A, B and C are subzones described in text. Mass gain and mass loss and the mobility of elements are indicated.

zone center (subzone-C) is characterized by massive volume gain. Episodic opening of veins in the shear zone center is likely to have set up a pressure gradient from the shear zone margins to the shear zone center. Material dissolved during the breakdown of feldspars migrated along pressure gradients towards the shear zone center (Fig. 9). Chemical softening due to feldspar breakdown (Hippertt, 1998; Ingles et al., 1999), the precipitation of quartz and grain size reduction lead to a change from brittle to ductile deformation regime and to the sealing of brittle structures.

(iii) Fluid overpressure is again built up during ongoing exhumation resulting in further fracturing of rocks and a new cycle is initiated. Migration of fluids along pressure gradients rather than temperature gradients is confirmed by a geochemical argument: Dipple and Ferry (1993) have shown that equilibrium fluid migration along temperature gradients can cause enrichment in Si and K but depletion of Na and Ca due to the temperature dependence of partitioning coefficients. However, these enrichments are incompatible with the enrichments and depletions of these four elements discussed above (Fig. 8d).

7.2. Some implications to regional geology

Type-I structures are characterized by a moderately north dipping mylonitic foliation and a west–east trending stretching lineation. Weak fabric asymmetries suggest major component of coaxial west–east stretch and north–south shortening. The same strain geometry with overall north–south shortening and west–east extension is obtained from the conjugate set of northwest trending dextral faults and northeast trending sinistral faults, defining the Type-II structures at Rossblei and Bromries. This stress regime is the same as that suggested by Neubauer et al. (1995) for the Cretaceous exhumation of the region. It is therefore suggested that the ore hosting shear zones and the synchronously formed mineralisations formed during the Eoalpine cycle. This is supported by (i) Ar–Ar ages of white mica grown in shear zones elsewhere in the Schladming Crystalline (Thöni, 1999); (ii) our *PT* estimates that are the same as those suggested for the Eoalpine metamorphic peak in the region (Hejl, 1997); and (iii) the salinity estimates reported here (Pohl and Belocky, 1999). This interpretation has some implication for the regional mapping results: At least some of these shear zones were formerly mapped as Permo-Mesozoic "quartz phyllite zones". However, the results from both geochemistry and

detailed structural observations confirm that the quartz phyllites are shear zones.

8. Conclusion

Structural and geochemical studies of polysulphide occurrences in the Schladming Crystalline Complex, Eastern Alps indicate that:

(1) Ore mineralisations is closely linked to the intersection of two different types of structures: (i) moderately north dipping shear zones with wide alteration zones and (ii) steep bundles of northwest–southeast and northeast–southwest striking carbonate filled faults.
(2) Geochemical and mineralogical profiling across the shear zones shows that they are characterized by silicification, sericitisation and carbonatisation in the central portions and by mass transfer from the margins of the shear zone to the center. These observations are best interpreted in terms of an acidic fluid infiltrating these structures.
(3) Sets of steep faults show no wall rock alteration but extensive carbonatisation. As there is no carbonate in the Schladming Crystalline, this observation is interpreted in terms of an external CO_2-bearing fluid that infiltrated these structures.
(4) Several stages of vein opening and subsequent deformation show that ore mineralisations and deformation occurred in a repeated and alternating process between brittle failure, ductile deformation and ore precipitation.
(5) Structural observations on the orientations of both types of structures and *PT* estimates for the formation conditions (350–400 °C and 3.5–4.5 kbar) indicate that the mineralisations formed most likely during the Cretaceous exhumation of the region.
(6) Structural, mineralogical and geochemical observations are consistent with a model of cyclic fluid infiltration. The migration of an acidic fluid from Type-I to Type-II structures and the migration of CO_2-bearing fluids in the opposite direction are interpreted as a cyclic transition between hydrostatic and lithostatic pressure and the build up and compensation of pressure gradients in different directions.

Acknowledgements

We are grateful to J. Loitzenbauer and K. Krenn for their support at the heating–freezing stage. We further acknowledge R. Abart for all the discussions on fluid–rock interaction and H. Werner for numerous field trips. P. Munchez and an anonymous reviewer are thanked for a range of useful comments on an earlier version of this manuscript. **[RR]**

References

Barnes, H.L., Seward, T.M., 1997. Geothermal systems and mercury deposits. In: Barnes, H.L. (Ed.), Geochemistry of Hydrothermal Ore Deposits. Wiley, New York, pp. 699–736.

Baumgartner, L.P., Olsen, S.N., 1995. A least-squares approach to mass transport calculations using the isocon method. Econ. Geol. 90, 1261–1270.

Bechtel, A., Gratzer, R., Puettmann, W., Oszczepalski, S., 2002. Geochemical characteristics across the oxic/anoxic interface (Rote Faeule front) within the Kupferschiefer of the Lubin–Sieroszowice mining district (SW Poland). Chem. Geol. 185, 9–31.

Bialek, D., 1999. Chemical changes associated with deformation of granites under greenschist facies conditions: the example of Zwaidó Granodiorite (SE Lusatian Granodirorite Complex, Poland). Tectonophysics 303, 251–261.

Brown, P.E., 1989. FLINCOR; a microcomputer program for the reduction and investigation of fluid-inclusion data. Am. Mineral. 74, 1390–1393.

Brown, P.E., Lamb, W.M., 1989. *P–V–T* properties of fluids in the system $H_2O–CO_2–NaCl$; new graphical presentations and implications for fluid inclusion studies. Geochim. Cosmochim. Acta 53, 1209–1221.

Burkhard, M., 1993. Calcite twins, their geometry, appearance and significance as stress–strain markers and indicators of tectonic regime: a review. J. Struct. Geol. 15, 355–368.

Cartwright, I., Buick, I.S., 1999. The flow of surface-derived fluids through Alice Springs age middle-crustal ductile shear zones, Reynolds Range, central Australia. J. Metamorph. Geol. 17, 397–414.

Christie, J.M., Ord, A., 1980. Flow stress from microstructures of mylonites: example and current assessment. J. Geophys. Res. 85, 6253–6262.

Craw, D., Windle, S.J., Angus, P.V., 1999. Gold mineralisation without quartz veins in a ductile–brittle shear zone, Macraes, Otago Schist, New Zealand. Miner. Depos. 34, 382–394.

Dipple, G.M., Ferry, J.M., 1993. Metasomatism and fluid flow in ductile fault zones. Contrib. Mineral. Petrol. 112, 149–164.

Dugdale, A.L., Hagemann, S.G., 2001. The Bronzewing lode-deposit, Western Australia: *P–T–X* evidence of fluid immiscibility caused by cyclic decompression in gold-bearing quartz veins. Chem. Geol. 173, 59–90.

Formanek, H.P., 1963. Zur Geologie und Petrologie der nordwestlichen Schladminger Tauern. Mitt. Ges. Geol.-Bergbaustud. 14, 9–81.

Friedrich, O.M., 1975. Monographie der Erzlagerstätten bei Schladming, III. Teil. Arch. Lagerstaettenforsch. Ostalpen 15, 29–63.

Frisch, W., Kuhlemann, J., Dunkl, I., Brügel, A., 1998. Palinspatic reconstruction and topographic evolution of the Eastern Alps during late tertiary Tectonic extrusion. Tectonophysics 297, 92–99.

Glasson, M.J., Keays, R.R., 1978. Gold mobilization during cleavage development in sedimentary rocks from the auriferous slate belt of central Victoria, Australia; some important boundary conditions. Econ. Geol. 73, 496–511.

Goddard, J.V., Evans, J.P., 1995. Chemical changes and fluid–rock interaction in faults of crystalline thrust sheets, northwestern Wyoming, USA. J. Struct. Geol. 17, 533–547.

Goldfarb, R.J., Leach, D.L., Miller, M.L., Pickthorn, W.J., 1986. Geology, metamorphic setting and genetic constraints on epigenetic lode-gold mineralisation within the Valdez Group, south central Alaska. In: Keppie, J.D., Boyle, R.W., Haynes, S.J. (Eds.), Turbidite-hosted Gold Deposits. Spec. Pap.-Geol. Assoc. Can., vol. 32, pp. 87–105.

Grant, J.A., 1986. The Isocon Diagram—a simple solution to Gresens Equation for Metasomatic Alteration. Econ. Geol. 81, 1976–1982.

Groves, D.I., 1993. The crustal continuum model for late-Archaean lode-gold deposits of the Yilgarn Block, Western Australia. Miner. Depos. 28, 366–374.

Hejl, E., 1997. "Cold Spots" during the Cenozoic evolution of the Eastern Alps: thermochronological interpretation of apatite fission-track data. Tectonophysics 272, 159–173.

Hippertt, J.F., 1998. Breakdown of feldspar, volume gain and lateral mass transfer during mylonitisation of granitoid in a low metamorphic shear zone. J. Struct. Geol. 20, 175–193.

Hirth, G., Tullis, J., 1992. Dislocation creep regimes in quartz aggregates. J. Struct. Geol. 20, 145–159.

Ingles, J., Lamouroux, C., Soula, J.C., Guerrero, N., Depat, P., 1999. Nucleation of ductile shear zones in a granodiorite under greenschist facies conditions, Beouvielle Massif, Pyrenees, France. J. Struct. Geol. 21, 555–576.

Kisters, A.F.M., Kolb, J., Meyer, M., Hoernes, S., 2000. Hydrologic segmentation of high-temperature shear zones: structural, geochemical and isotopic evidence from auriferous mylonites of Renco mine, Zimbabwe. J. Struct. Geol. 22, 811–829.

Köppel, V., Neubauer, F., Schroll, E., 1993. Pre-Alpidic Ore Deposits in the Central, Eastern and Southern Alps. In: von Raumer, J.F., Neubauer, F. (Eds.), Pre-Mesozoic Geology in the Alps. Springer, Berlin, pp. 145–162.

Kretz, R., 1983. Symbols for rock forming minerals. Am. Mineral. 68, 277–279.

Liu, W., McPhail, D.C., Brugger, J., 2001. An experimental study of copper(I)–chloride and copper(I)–acetate complexing in hydrothermal solutions between 50 °C and 250 °C and vapor-saturated pressure. Geochim. Cosmochim. Acta 65, 1227–1243.

Mandl, G., Matura, A., 1995. Geologische Karte der Republik Österreich, Blatt 127 Schladming. Österreichische Geologische Bundesanstalt, Wien.

Matura, A., 1987. Schladminger Kristallinkomplex. In: Matura, A. (Ed.), Arbeitstagung der geologischen Bundesanstalten 1987—Blatt 127 Schladming ÖGG, pp. 13–24.

McCuaig, T.C., Kerrich, R., 1998. $P-T-t$ deformation—fluid characteristics of lode gold deposits: evidence from alteration systematics. Ore Geol. Rev. 12, 381–458.

Mikucki, E.J., 1998. Hydrothermal transport and depositional processes in Archean lode-gold systems; a review. Ore Geol. Rev. 13, 307–321.

Müller, B., Seward, T.M., 2001. Spectrophotometric determination of the stability of tin(II) chloride complexes in aquous solutions up to 300 °C. Geochim. Cosmochim. Acta 65, 4187–4199.

Neubauer, F., Frisch, W., 1993. The Austroalpine Metamorphic Basement East of the Tauern Window. In: von Raumer, J.F., Neubauer, F. (Eds.), Pre-mesozoic Geology in the Alps. Springer, Berlin, pp. 515–536.

Neubauer, F., Dallmeyer, R.D., Dunkl, I., Schirnik, D., 1995. Late Cretaceous exhumation of the metamorphic Gleinalm Dome, Eastern Alps: kinematics, cooling history and sedimentary response in a sinistral wrench corridor. Tectonophysics 242, 79–98.

Newman, J., Mitra, G., 1993. Lateral variations in mylonite zone thickness as influenced by fluid–rock interaction, Linville Falls faults, North Carolina. J. Struct. Geol. 15, 849–863.

Nguyen, P.T., Cox, S.F., Harris, L.B., Powell, C.M., 1998. Fault-valve behaviour in optimally oriented shear zones: an example at Revenge gold mine, Kambalda, Western Australia. J. Struct. Geol. 20, 1625–1640.

O'Hara, K.D., 1988. Fluid flow and volume loss during mylonitisation: an origin for phyllonite in an overthrust setting, North Carolina, U.S.A. Tectonophysics 156, 21–36.

Okudaira, T., Takeshita, T., Hara, I., Ando, J., 1995. A new estimate of the conditions for tranistion from basal <a> to prism [c] slip in naturally deformed quartz. Tectonophysics 250, 31–46.

Oliver, N.H.S., 2001. Linking of regional and local hydrothermal systems in the mid-crust by shearing and faulting. Tectonophysics 335, 147–161.

Peacock, S.M., 1989. Numerical constraints on rates of metamorphism and fluid production and fluid flux during regional metamorphism. Geol. Soc. Amer. Bull. 101, 476–485.

Pettke, T., Diamond, L.W., Kramers, J.D., 2000. Mesothermal gold lodes in the north-western Alps; a review of genetic constraints from radiogenic isotopes. Eur. J. Mineral. 12, 213–230.

Piessens, K., Muchez, P., Dewaele, S., Boyce, A., De Vos, W., Sintubin, M., Debacker, T.N., Burke, E.A.J., Viaene, W., 2002. Fluid flow, alteration and polysulphide mineralistation associated with low-angle reverse shear zone in the Lower Palaeozoic of the Anglo-Brabant fold belt, Belgium. Tectonophysics 348, 72–92.

Pohl, W., Belocky, R., 1999. Metamorphism and metallogeny in the Eastern Alps. Miner. Depos. 34, 614–629.

Reed, M.H., 1997. Hydrothermal alteration and its relationship to Ore Fluid Composition. In: Barnes, H.L. (Ed.), Geochemistry of Hydrothermal Ore Deposits. Wiley, New York, pp. 303–365.

Schermaier, A., Haunschmid, B., Finger, F., 1997. Distribution of

variscan I- and S-type granites in the Eastern Alps: a possible clue to unravel pre-Alpine basement structures. Tectonophysics 272, 315–333.

Selverstone, J., Morteani, G., Staude, J.M., 1991. Fluid channeling during ductile shearing: transformation of granodiorite into aluminous schists in the Tauern Window, Eastern Alps. J. Metamorph. Geol. 9, 419–431.

Seward, T.M., Barnes, H.L., 1997. Metal transport by hydrothermal ore fluids. In: Barnes, H.L. (Ed.), Geochemistry of Hydrothermal Ore Deposits. Wiley, New York, pp. 435–486.

Sibson, R.H., Robert, F., Poulsen, K.H., 1988. High-angle reverse faults, fluid-pressure cycling, and mesothermal gold-quartz deposits. Geology 16, 551–555.

Slapansky, P., Frank, W., 1987. Structural evolution and geochronology of the Northern Margin of the Austroalpine in the northwestern Schladming Crystalline (NE Radstätter Tauern). In: Flügel, H.W., Faupl, P. (Eds.), Geodynamics of the Eastern Alps. Deutike, Vienna, pp. 237–262.

Stüwe, K., 1998. Tectonic constraints on the timing relationships of metamorphism, fluid production and gold-bearing quartz vein emplacement. Ore Geol. Rev. 13, 219–228.

Thöni, M., 1999. A review of geochronological data from the Eastern Alps. Schweiz. Mineral. Petrogr. Mitt. 79, 209–230.

Tourigny, G., Tremblay, A., 1997. Origin and incremental evolution of brittle/ductile shear zones in granitic rocks: natural examples from southern Abitibi Belt, Canada. J. Struct. Geol. 20, 799–818.

Wang, X., Neubauer, F., 1997. Orogen-parallel strike-slip faults bordering metamorphic core complexes: the Salzach–Enns fault zone in the Eastern Alps, Austria. J. Struct. Geol. 20, 799–818.

Weiss, A., 1987. Zur Geschichte des Schladminger Bergbaues. In: Matura, A. (Ed.), Arbeitstagung der geologischen Bundesanstalten 1987—Blatt 127 Schladming ÖGG, pp. 118–123.

Wibberly, C., 1999. Are feldspar-to-mica reactions necessarily reaction-softening processes in fault zones? J. Struct. Geol. 21, 1219–1227.

Yang, X.Y., O'Hara, K.D., Moecher, D.P., 1998. Distinction between tectonic mixing and mass transfer processes in a ductile shear zone. J. Struct. Geol. 20, 1089–1103.

Zulauf, G., Palm, S., Petschick, R., Spies, O., 1999. Element mobility and volumetric strain in brittle and brittle–viscous shear zones of the superdeep well KTB (Germany). Chem. Geol. 156, 135–149.